Journal of Physics and Chemistry of Solids 114 (2018) 141–152

Contents lists available at ScienceDirect

Journal of Physics and Chemistry of Solids

journal homepage: www.elsevier.com/locate/jpcs

Experimental and theoretical study to explain the morphology of $CaMoO_4$ crystals

F.K.F. Oliveira [a], M.C. Oliveira [b], L. Gracia [c], R.L. Tranquilin [a], C.A. Paskocimas [a], F.V. Motta [a], E. Longo [d], J. Andrés [b], M.R.D. Bomio [a,*]

[a] LSQM- Laboratório de Síntese Química de Materiais, DEMat, Universidade Federal do Rio Grande do Norte - UFRN, P.O. Box 1524, 59078-970 Natal, RN, Brazil
[b] Departament de Química Física i Analítica, Universitat Jaume I, 12071 Castelló de la Plana, Spain
[c] Department of Physical Chemistry, University of Valencia, 46100 Burjassot, Spain
[d] CDMF-UFSCar, Universidade Federal de São Carlos, P.O. Box 676, 13565-905 São Carlos, SP, Brazil

ARTICLE INFO

Keywords:
$CaMoO_4$
Microwave-assisted hydrothermal method
Morphology
Wulff construction

ABSTRACT

$CaMoO_4$ crystals were prepared by a controlled co-precipitation method and processed in a domestic microwave-assisted hydrothermal system with two different surfactants (ethyl 4-dimethylaminobenzoate and 1,2,4,5-benzenetetracarboxylic dianhydride). The corresponding structures were characterized by X-ray diffraction and Rietveld refinement techniques, Fourier transform infrared spectroscopy, ultraviolet–visible absorption spectroscopy, and photoluminescence measurements. Field emission scanning electron microscopy was used to investigate the morphology of the as-synthesized aggregates. The structure, the surface stability of the (001), (112), (100), (110), (101), and (111) surfaces of $CaMoO_4$, and their morphological transformations were investigated through systematic first-principles calculations within the density functional theory method at the B3LYP level. Analysis of the surface structures showed that the electronic properties were associated with the presence of undercoordinated $[CaO_x]$ ($x = 5$ and 6) and $[MoO_y]$ ($y = 4$ and 3) clusters. The relative surfaces energies were tuned to predict a complete map of the morphologies available through a Wulff construction approach. The results reveal that the experimental and theoretical morphologies obtained coincide when the surface energies of the (001) and (101) surfaces increase, while the surface energy of the (100) facet decreases simultaneously. The results provide a comprehensive catalog of the morphologies most likely to be present under realistic conditions, and will serve as a starting point for future studies on the surface chemistry of $CaMoO_4$ crystals.

1. Introduction

Calcium molybdate ($CaMoO_4$) belongs to the scheelite family with its $AMoO_4$ formula, where A is Ca, Sr, or Ba, and has a tetragonal structure with space group $I4_1/a$ [1,2]. This type of structure is composed of dodecahedral $[CaO_8]$ clusters and tetrahedral $[MoO_4]$ clusters connected via common vertices. In turn, $[CaO_8]$ polyhedra are connected via the edges and form a 3D framework [2–4] in which the Ca—O—Mo moiety can act as a "hinge," allowing the $[MoO_4]$ cluster more rotational freedom [5] to generate a structural disorder at the $[CaO_8]$ and $[MoO_4]$ clusters throughout the scheelite lattice [6,7].

$CaMoO_4$ (nano)crystals have received great attention, and many different preparation methods have been reported, such as solid-state reaction [8,9], citrate complex methods [10,11], a galvanic cell method [12], sol-gel methods [13,14], an ultrasound method [15], hydrothermal methods [16,17], a free surfactant sonochemical method [18], chemical deposition [19–22], precipitation [23], co-precipitation [24–27], and microwave-hydrothermal [2,11,28–33]. From the theoretical point of view, the geometry, electronic properties, and optical properties of $CaMoO_4$ have been investigated by density functional theory (DFT) methods [34–36].

In recent years, the search for the relationship between morphology and properties has attracted increasing attention to the field of material research. The performance of various crystal facets is linked to unique surface features such as local electronic structure [37], atomic termination [38], atomic population [39], coordination patterns [40], dangling

* Corresponding author.
E-mail address: mauricio.bomio@ct.ufrn.br (M.R.D. Bomio).

https://doi.org/10.1016/j.jpcs.2017.11.019
Received 20 June 2017; Received in revised form 22 November 2017; Accepted 24 November 2017
Available online 26 November 2017

bonds [41], and internal electric strain [42], as well as surface energies [43]. Particularly, the activity of nanocrystals used as catalysts depends strongly on the surface structure of facets enclosing these crystals [44–49], and makes it possible to increase catalytic activity and selectivity by optimization of the structure of the catalytically active site. In addition, according to Ruditskiy et al. [50], the shape control of nanocatalysts helps to optimize the catalytic applicability and reduces the costs of the material. Therefore, changing the morphology of the as-synthesized (nano)crystals and further controlling their properties are great challenges for their application. However, the control of the final morphology and surface structure, which is a complex and difficult task, is highly dependent on the crystal internal structures, synthesis method, and external growth conditions, such as the concentration of the constituents, surfactants, additives, solvents, etc. In this study, surface energies of six different surfaces, (001), (112), (110), (101), (100), and (111), of the $CaMoO_4$ crystal were calculated with use of DFT. The predominant cleavage surfaces, the preferentially expressed crystal surfaces, and the corresponding morphologies were predicted theoretically, and these were then compared with the observations based on field emission scanning electron microscopy (FE-SEM) images.

In this work, we seek to fulfill a twofold objective. Firstly, the synthesis and characterization of $CaMoO_4$ crystals was done with and without different surfactants (ethyl 4-dimethylaminobenzoate [EDA] and 1,2,4,5-benzenetetracarboxylic dianhydride [BTD]) by a co-precipitation method and with processing in a domestic microwave-assisted hydrothermal system at 140 °C for 1, 2, 4, and 8 min. These samples were structurally characterized by X-ray diffraction (XRD), Fourier transform infrared (FT-IR) spectroscopy, FE-SEM, ultraviolet–visible (UV–vis) absorption spectroscopy, and photoluminescence (PL) measurements. Secondly, we intend to provide detailed microscopic information on the evolution of the final morphology with the surfactant used throughout the synthesis. Shape control was achieved by precise tuning of the experimental parameters, such as the presence of surfactants and time.

We believe that these results can arouse enough interest since they will contribute to broadening of the fundamental knowledge of the morphology of compounds based on $CaMoO_4$. To do so, a recent experimental and theoretical strategy was applied, based on the joint use of experimental findings and first-principles calculations at the DFT level. The Wulff construction is used to obtain the electronic, structural, and energetic properties that control the morphology and the transformation mechanism of metals, binary oxides, and complex crystals [51–54]. This strategy was recently used in $BaWO_4$ [55], $BaMoO_4$ [56], and α-$AgVO_3$ [57] crystals. In this context, Ng and Fan [58] reported a simple method to prepare uniform β-Ag_2MoO_4 crystals with well-defined shapes, which is expected to catalyze more extensive studies on the photocatalytic properties of the material.

This work follows this procedure to obtain a complete map of available morphologies for $CaMoO_4$ crystals. In addition, on the basis of these results, we are able to rationalize how the different surfaces change their energies throughout the synthesis process, and we are able to propose a path by which the experimental and theoretical morphologies of $CaMoO_4$ can match. With corrected surface energies, a straightforward understanding was provided by Wulff construction.

The rest of the article is divided into three sections. In the next section, we describe, in detail, the materials and methods for synthesizing and processing $CaMoO_4$ powders, as well as the computational method and model systems used to perform the first-principles calculations. Section 3 contains the results and discussion. The article ends with the main conclusions of our work.

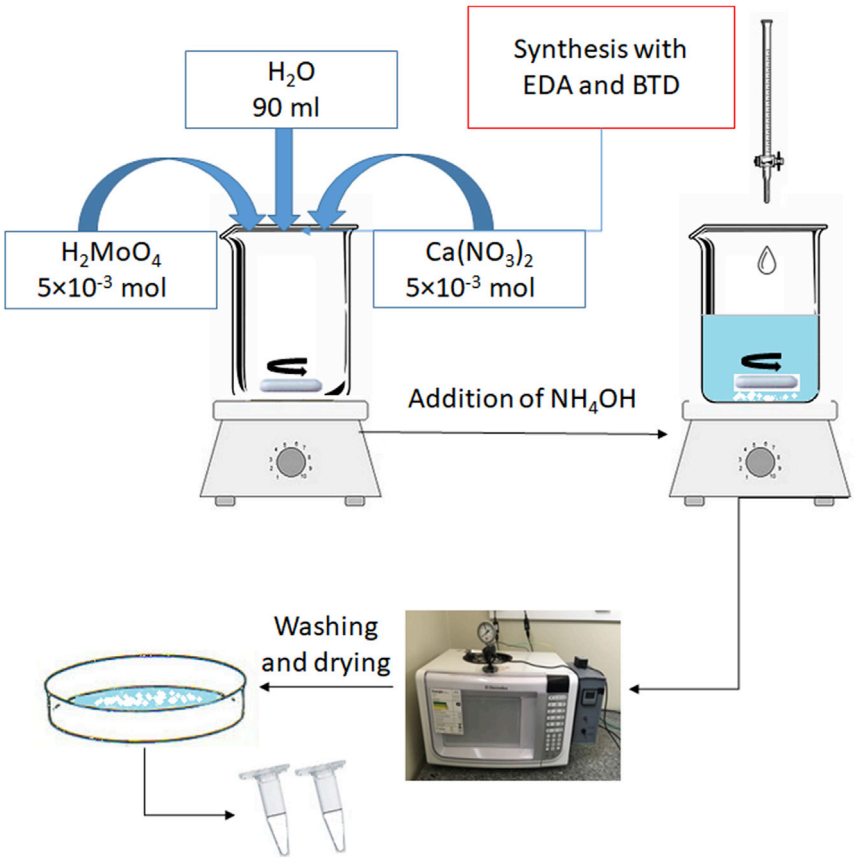

Fig. 1. The synthesis process for $CaMoO_4$ crystals. BTD, 1,2,4,5-benzenetetracarboxylic dianhydride; EDA, ethyl 4-dimethylaminobenzoate.

2. Materials and methods

2.1. Synthesis and processing of $CaMoO_4$ powders

$CaMoO_4$ powders were synthesized by a co-precipitation method in distilled water and processed in a microwave-assisted hydrothermal system for different times (1, 2, 4, and 8 min). Two different surfactants were used during the synthesis: Ethyl 4-dimethylaminobenzoate (EDA) and 1,2,4,5-benzenetetracarboxylic dianhydride (BTD). In addition, the samples were also synthesized without the surfactant, as a reference. A schematic representation of the synthesis of $CaMoO_4$ crystals is illustrated in Fig. 1.

A typical experimental procedure was as follows: 5×10^{-3} mol of molybdic acid, H_2MoO_4 (85%purity, Synth), and 5×10^{-3} mol of calcium nitrate, $Ca(NO_3)_2$ (99.5% purity, Sigma-Aldrich), were dissolved in 90 mL of water, and the mixture was stirred for 15 min. Then 5 mL of ammonium hydroxide, NH_4OH, was added to this solution until the pH reached 14 to intensify the rate of hydrolysis between Mo and Ca ions, as shown in Eqs. (1) and (2):

$$H_2MoO_{4\,(s)} + Ca(NO_3)_{2\,(s)} \xrightarrow{H_2O} 2H^+_{(aq)} + 2NO^-_{3\,(aq)} + Ca^{2+}_{(aq)} + MoO^{2-}_{4\,(aq)} \quad (1)$$

$$Ca^{2+}_{(aq)} + MoO^{2-}_{4\,(aq)} \rightarrow CaMoO_{4\,(s)} \quad (2)$$

Subsequently, processing was done with a microwave-assisted hydrothermal system (2.45 GHz, maximum power of 800 W). The solution was transferred into a Teflon autoclave and processed at 140 °C for 1, 2, 4, and 8 min. The pressure into the autoclave was stabilized at 3.4 bar. The solution obtained was washed with distilled water ten times to neutralize the solution (pH ≈ 7). Finally, the precipitates were dried at 100 °C for 24 h.

2.2. Characterizations of $CaMoO_4$ powders

$CaMoO_4$ powders were structurally characterized by XRD patterns, which were obtained with a Bruker/D2 PHASER with Cu-Kα radiation in the 2θ range from 10° to 75° at a rate of 0.02°/min. The lattice parameters a and c were calculated by adjustment of the experimental diffractogram with use of the program MAUD [56]. The average crystallite sizes and microstrain were calculated by the Williamson-Hall method [59–61].

FT-IR spectra were recorded at room temperature with a Shimadzu IRTracer-100 instrument. The morphology of the powders was observed by FE-SEM (Zeiss Auriga). UV–vis spectra were recorded with a Shimadzu UV-2600 spectrophotometer in reflectance mode. PL spectra were measured with a Thermo Jarrell Ash Monospec 27 monochromator and a Hamamatsu R446 photomultiplier. The 350.7 nm line of a krypton ion laser (Coherent Innova 90 K) was used as the excitation source, with the output power of the laser kept at 200 mW. All measurements were taken

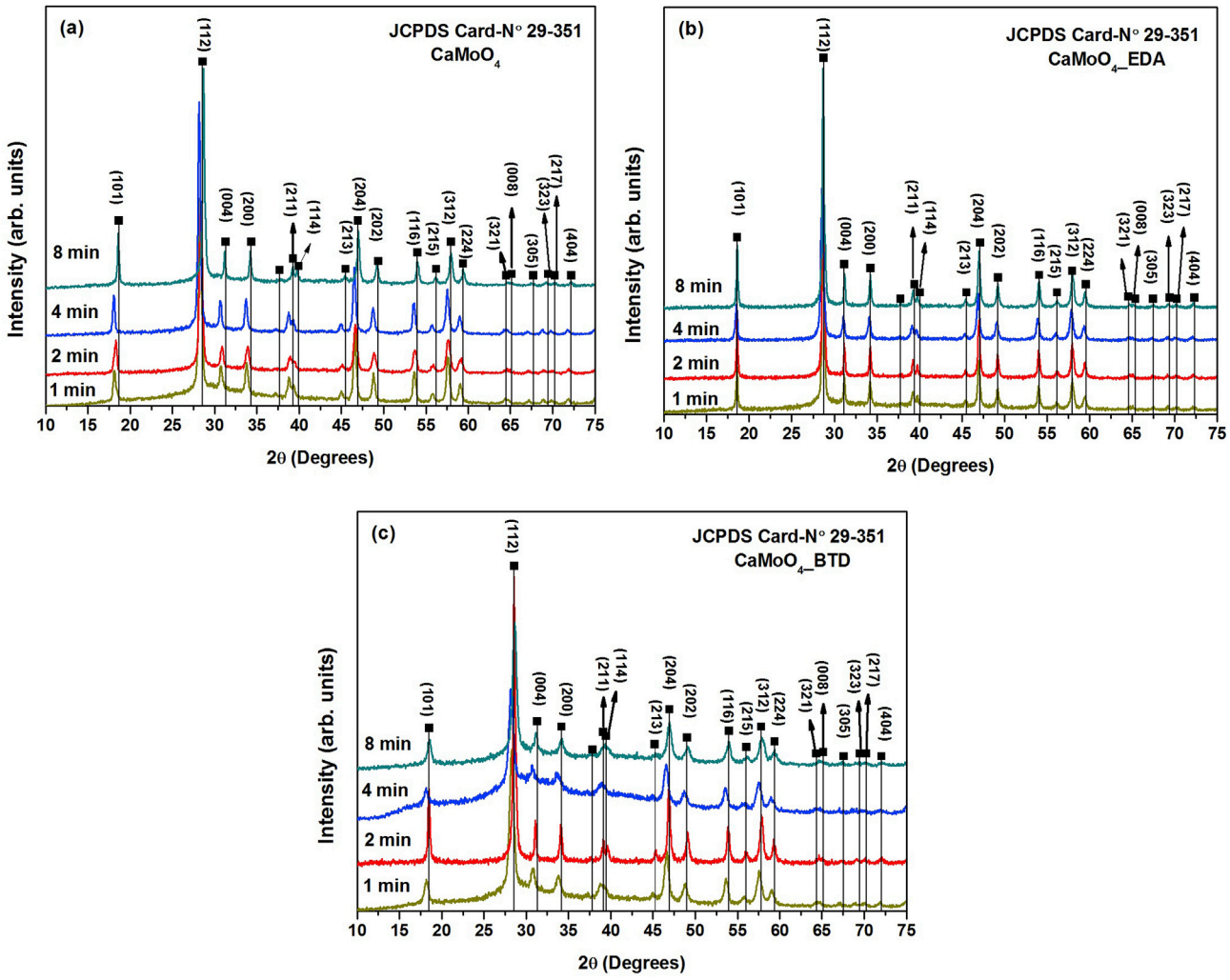

Fig. 2. X-ray diffraction patterns of $CaMoO_4$ crystals at 1, 2, 4, and 8 min: (a) $CaMoO_4$, (b) $CaMoO_4$ prepared with ethyl 4-dimethylaminobenzoate, and (c) $CaMoO_4$ prepared with 1,2,4,5-benzenetetracarboxylic dianhydride.

at room temperature.

2.3. Computational method

Theoretical procedures and computational methods involving first-principles calculations related to the $CaMoO_4$ structure were performed with the hybrid functional B3LYP and the periodic DFT framework [62,63] with use of the CRYSTAL14 software package [64].

Mo cations [65] were described by a pseudopotential basis set, while O anions [66] and Ca cations [67] were described by standard (6-31d1G) basis sets.

For bulk and surface calculations, the diagonalization of the Fock matrix was performed at adequate *k*-point grids in the reciprocal space. The thresholds controlling the accuracy of the calculation of the Coulomb and exchange integrals were set to 10^{-8} (ITOL1 to ITOL4) and 10^{-14} (ITOL5), and the percentage of mixing Fock/Kohn-Sham matrices was set to 40 (IPMIX keyword) [68].

Surface energies were determined from the equilibrium shape by a classic Wulff construction [69] that minimizes the total surface free energy at a fixed volume, providing a simple correlation between the surface energy (E_{surf}) of the (*hkl*) plane and the distance (r_{hkl}) in the normal direction from the center of the crystallite. The Wulff construction has been successfully used in materials science to obtain the morphology of materials, including $PbMoO_4$, $CaWO_4$, Ag_3PO_4, α-Ag_2MoO_4, $BaMoO_4$, $BaWO_4$, Ag_2CrO_4, and $LaVO_4$ [54,56,70–75]. The surface energy (E_{surf}) is defined as the total energy per repeating slab cell (E_{slab}) minus the total energy of the perfect crystal per molecular unit ($E_{bulk/atom}$) multiplied by the number of molecular units of the surface (N_s) and divided by the surface area per repeating cell of the two sides of the slab.

3. Results and discussion

3.1. XRD analyses

Fig. 2 show the XRD patterns obtained at different times (1, 2, 4, and 8 min) for $CaMoO_4$ powders processed in a microwave-assisted hydrothermal system at 140 °C. The XRD patterns revealed that all diffraction peaks of $CaMoO_4$ powders can be indexed to the scheelite-type tetragonal structure without the presence of secondary phases, in agreement with Joint Committee on Powder Diffraction Standards (JCPDS) card no. 29-351 [76]. Moreover, the relative intensities and sharp diffraction of all peaks indicated that the materials are well crystallized, suggesting an ordered structure at long range.

3.2. Rietveld refinement analysis

The Rietveld method is based on the construction of diffraction patterns calculated according to the structural model [77]. The Rietveld refinement was performed with MAUD [78], and the refined parameters were the lattice parameters, background, profile, half-width parameters (*u*, *v*, *w*), and crystallite size [79]. The results for all the powders were obtained by the Rietveld method with use of Crystallography Open Database entry 9009632 [80]. Table 1 shows the lattice parameters, cell volume, and positions of the atoms. An analysis of the results reveals small differences with the reported data [80]. Nevertheless, it is important to note the variations in the position of the oxygen anions (Table 2). These variations are associated with distortions of the Ca—O and/or Mo—O bond lengths, and consequently with different levels of distortion of the $[CaO_8]$ and/or $[MoO_4]$ clusters in the lattice.

The $CaMoO_4$ microstrain (ε_{hkl}) and crystallite sizes (D_{hkl}) were analyzed by the Williamson-Hall method. It is represented by Eq. (3):

$$\frac{\beta_{hkl}\cos\theta}{\lambda} = \frac{1}{D_{hkl}} + \frac{(\varepsilon_{hkl})\varepsilon\sin\theta}{\lambda} \quad (3)$$

where β_{hkl} is the full width at half maxima (FWHM) of XRD patterns, θ is the diffraction angle, λ is the wavelength of the X-Rays, D_{hkl} is the average crystallite size, and ε_{hkl} is the micro-strain.

Table 1 and Fig. S1, Fig.S2, and Fig.S3 show the results for crystallite size and microstrain for pure $CaMoO_4$, $CaMoO_4$ prepared with EDA ($CaMoO_4$_EDA), and $CaMoO_4$ prepared with BTD ($CaMoO_4$_BTD) obtained at different processing times of 1, 2, 4, and 8 min in the microwave-assisted hydrothermal system at 140 °C. For $CaMoO_4$ samples, a large difference in crystallite size and microstrain was not observed. For $CaMoO_4$_EAD processed at 140 °C for 8 min, the crystallite size and microstrain increase, probably due to distortion in the crystalline lattice promoted by the surfactant EDA. For $CaMoO_4$_BTD processed at 140 °C for 1 and 2 min, we can conclude that the surfactant BTD acts as a

Table 1
Rietveld refinement and Williamson-Hall data for the as-synthesized $CaMoO_4$ crystals.

Sample	*t* (min)	*a* (Å)	*c* (Å)	*V* (Å^3)	D_{hkl} (nm)	$\mathcal{E}_{hkl}$
$CaMoO_4$	1	5.235	11.458	314.05	46	0.003
	2	5.220	11.428	311.42	41	0.003
	4	5.233	11.451	313.56	30	0.002
	8	5.225	11.437	312.25	34	0.003
$CaMoO_4$ (EDA)	1	5.234	11.454	313.71	40	0.003
	2	5.235	11.456	313.94	43	0.002
	4	5.235	11.457	313.98	36	0.003
	8	5.234	11.453	313.75	66	0.004
$CaMoO_4$ (BTD)	1	5.225	11.432	312.11	27	0.003
	2	5.237	11.459	314.22	34	0.002
	4	5.227	11.433	312.52	30	0.004
	8	5.236	11.458	314.16	43	0.006
COD entry	9009632	5.222	11.425	314.16	–	–

t is the synthesis time, *a* and *c* are lattice parameters, *V* is the unit cell volume, D_{hkl} is the average crystallite size, and $\mathcal{E}_{hkl}$ is the microstrain.
BTD, 1,2,4,5-benzenetetracarboxylic dianhydride; COD, Crystallography Open Database; EDA, ethyl 4-dimethylaminobenzoate.

Table 2
Atomic coordinates for $CaMoO_4$ crystalline structures.

Sample	*t* (min)	Atom	*x*	*y*	*z*
$CaMoO_4$	1	Ca	0	0.25	0.625
		Mo	0	0.25	0.125
		O	0.1553	−0.00767	0.208195
	2	Ca	0	0.25	0.625
		Mo	0	0.25	0.125
		O	0.149	0.0069	0.2089
	4	Ca	0	0.25	0.625
		Mo	0	0.25	0.125
		O	0.1569	−0.03105	0.206959
	8	Ca	0	0.25	0.625
		Mo	0	0.25	0.125
		O	0.15834	−0.04248	0.21528
$CaMoO_4$ (EDA)	1	Ca	0	0.25	0.625
		Mo	0	0.25	0.125
		O	0.15561	−0.01478	0.20835
	2	Ca	0	0.25	0.625
		Mo	0	0.25	0.125
		O	0.15246	−0.00021	0.20929
	4	Ca	0	0.25	0.625
		Mo	0	0.25	0.125
		O	0.15403	−0.0172	0.20952
	8	Ca	0	0.25	0.625
		Mo	0	0.25	0.125
		O	0.15309	−0.00562	0.20944
$CaMoO_4$ (BTD)	1	Ca	0	0.25	0.625
		Mo	0	0.25	0.125
		O	0.14878	−0.05927	0.206735
	2	Ca	0	0.25	0.625
		Mo	0	0.25	0.125
		O	0.15667	−0.00845	0.20904
	4	Ca	0	0.25	0.625
		Mo	0	0.25	0.125
		O	0.17313	−0.04003	0.214182
	8	Ca	0	0.25	0.625
		Mo	0	0.25	0.125
		O	0.15335	−0.02341	0.204194

BTD, 1,2,4,5-benzenetetracarboxylic dianhydride; EDA, ethyl 4-dimethylaminobenzoate.

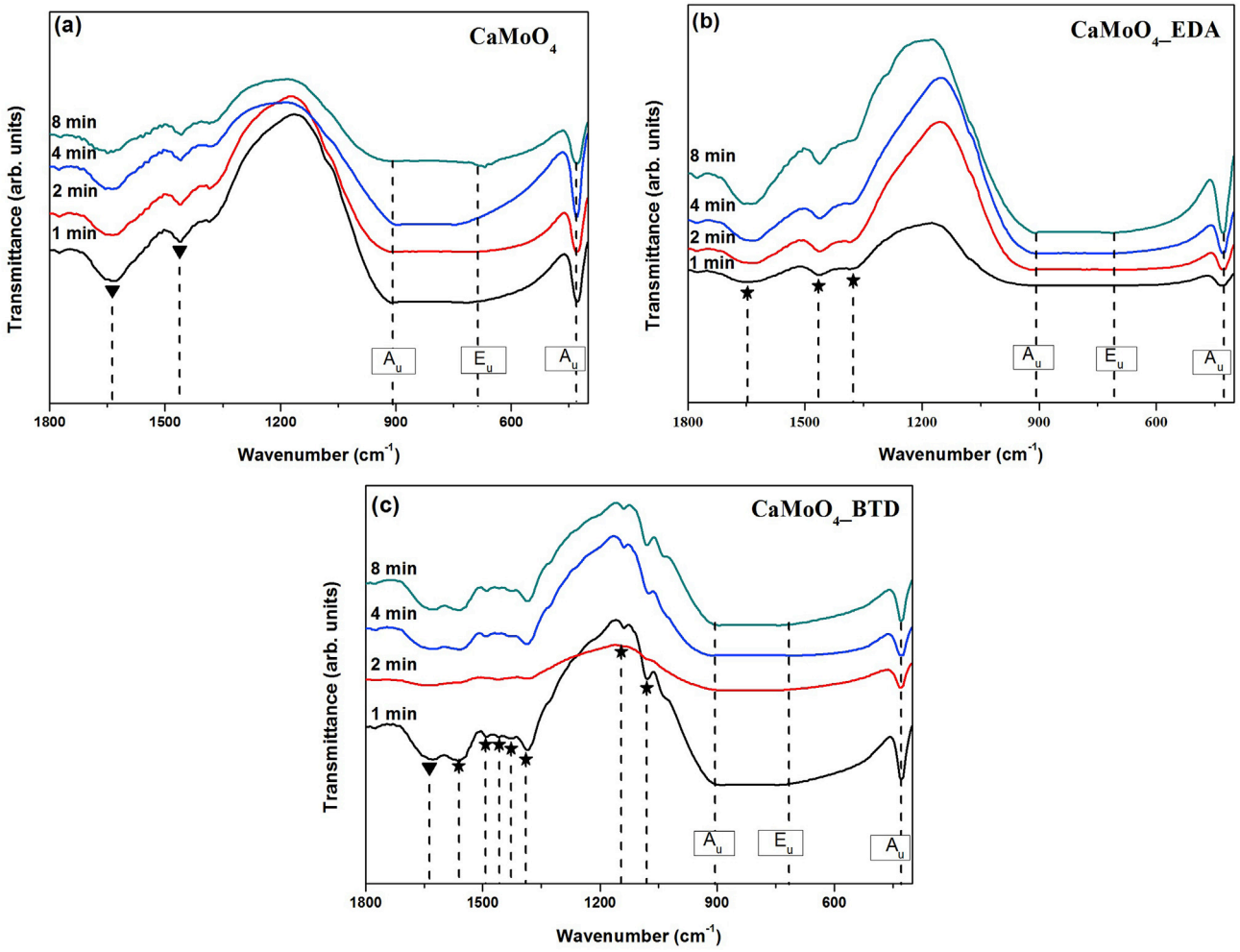

Fig. 3. Fourier transform infrared patterns of $CaMoO_4$ crystals at 1, 2, 4, and 8 min: (a) $CaMoO_4$, (b) $CaMoO_4$ prepared with ethyl 4-dimethylaminobenzoate ($CaMoO_4$_EDA), and (c) $CaMoO_4$ prepared with 1,2,4,5-benzenetetracarboxylic dianhydride ($CaMoO_4$_BTD).

Table 3
Experimental and theoretical results for Raman-active and infrared-active modes (cm^{-1}) of $CaMoO_4$.

Raman Experimental												
B_g	Eg	Eg	Ag	Bg	Eg	Ag	Bg	B_g	E_g	Eg	B_g	A_g
–	–	–	205	–	263	333	339	393	401	797	844	878 [78]
110	145	189	205	219	263	333	339	393	401	797	844	878 [80]
112	143	190	205	214	267	322	328	391	402	792	845	877 [81]
111.5	143	189.5	204.5	214	267	321.5	327.5	391	402.5	792	845.5	877 [83]
111	145	189	205	–	267	323	–	391	402	793	847	878 [82]
Theoretical												
116.8	159.8	196.6	226.5	231.7	303.6	337.3	346.3	432.5	441	819.5	864.5	896[a]
Infrared												
Experimental												
E_u	Au	Eu	Au	Eu	Au	Au	Eu					
–	–	–	–	–	430	–	820 [79]					
–	–	–	–	405	430	–	827 [7]					
–	–	240	280	330	428	790	878 [1]					
–	–	–	–	–	411–423	720–970 [26]						
–	–	–	–	–	423	743–895 [32]						
–	–	–	–	–	430	790–900[a]						
Theoretical												
158.8	195.3	209.1	250.7	327.5	470.7	785.3	808.7[a]					

[a] Present work.

growth control agent because of the smaller crystallites than for pure $CaMoO_4$. On the other hand, for $CaMoO_4$_BTD processed at 140 °C for 4 and 8 min, BTD enhances the lattice distortion parameter *c*.

3.3. FT-IR analysis

The scheelite-type tetragonal structure exhibits 26 different vibration modes: ($\Gamma = 3A_g + 5A_u + 5B_g + 3B_u + 5E_g + 5E_u$), but eight of them ($4A_u$ and $4E_u$) are active in the infrared, while the other 13 modes (A_g, B_g, and E_g) are Raman active [81].

Fig. 3 shows the FT-IR spectra of the $CaMoO_4$ crystals in the range from 1800 to 400 cm^{-1}. Three types of vibration modes are seen ($1E_u$ and $2A_u$), while the other vibration modes are not identified because they are located in the lower region (400–100 cm^{-1}). An analysis of the results reveals the presence of an intense absorption band, around 660–910 cm^{-1}, corresponding to E_u and A_u modes that are associated with the antisymmetric stretch of the tetrahedral [MoO_4] clusters. At 432 cm^{-1}, a less intense A_u mode, corresponding to antisymmetric vibrations of the O—Mo—O angles, is observed. However, in FT-IR analysis it is possible to perceive some differences in the simple $CaMoO_4$. In Fig. 3(a), the peaks between 1630 and 1450 cm^{-1} are attributed to the presence of CO_2 in the atmosphere [1], while in Fig. 3(b), the peak around 1357 cm^{-1} is assigned to the presence of a tertiary amine organic group resulting from EDA. In Fig. 3(c), in the region from 1380 to 560 cm^{-1}, the vibration corresponding to the out-of-plane bending of CH_2 is observed, while the wide band between 1134 and 1070 cm^{-1} is associated with the presence of anhydride [C—C(=O)—O—C(=O)—C] groups from BTD. At 1650 cm^{-1}, a band associated with the O—H bond of the water molecule was identified [82], while at 1450 cm^{-1}, a band corresponding to C—O bonds was identified [1,2].

The theoretical and experimental frequencies for the infrared and Raman spectra are shown in Table 3, and the comparison and analysis of the results shows they are agreement with the results previously reported in the literature [1,2,26,32,81–86].

Theoretical analysis predicts that seven of these modes ($2A_g + 3B_g + 2E_g$) are internal motions of tetrahedral [MoO_4] clusters and octahedral [CaO_8] clusters, while the other six ($1A_g + 2B_g + 3E_g$) are external pure lattice modes of the [MoO_4] tetrahedra (translational and rotational motions between ions in the lattice) [87]. In principle, there is a strong interaction between the O—Ca—O and O—Mo—O moieties of adjacent clusters, which are structurally ordered at short range; and intense and sharp bands are exhibited at low intensities as observed at 116.8 cm^{-1} (B_g) and 159.8 and 196.6 cm^{-1} (E_g). Internal motions of MoO_4 tetrahedra such as symmetric bending at 441.0 cm^{-1} (E_g) and 432.5 cm^{-1} (B_g) or antisymmetric bending at 346.3 cm^{-1} (B_g), 337.3 cm^{-1} (A_g), 303.6 cm^{-1} (E_g), and 231.7 cm^{-1} (B_g) can be observed. However, strong intense bands at 896.0, 864.5, and 819.5 cm^{-1} are attributed to internal/optical modes A_g, B_g, and E_g, respectively. The A_g mode was observed at 896.0 cm^{-1} and was assigned to symmetric stretching vibrations of [MoO_4] clusters, and the B_g and E_g modes at 864.5 and 819.5 cm^{-1} were assigned to antisymmetric stretching vibrations of the O—Mo—O moieties (Fig. 4).

3.4. UV–vis analysis

The optical band gap energy (E_{gap}) was calculated by the method proposed by Wood and Tauc [88]. The band gap energy for all $CaMoO_4$ particles synthesized at 140 °C for different times, with and without surfactants, was calculated, and the values are listed in Table 4 and Fig. S4, Fig.S5, and Fig.S6.

Roca et al. [89]. describe that the exponential optical absorption profile and E_{gap} are controlled by the degree of structural order-disorder in the lattice. In our study, the UV–vis spectra evidenced changes of band gap energies with the increase of the heating time. The results agree with those reported in the literature [1,2] regarding the presence of intermediary energy levels between the valence band and the conduction band [72,85,90]. The formation of this intermediate energy level inside the band gap can be described by the degree of order and disorder of the crystalline structure [90]. Therefore, as can be seen in Tables 1 and 4, the increase in structural disorder and the volume of $CaMoO_4$ synthesized in presence of EDA promotes a wide intermediate level compared with the pure $CaMoO_4$ and $CaMoO_4$_BTD, having as a consequence a reduction in the band gap energy.

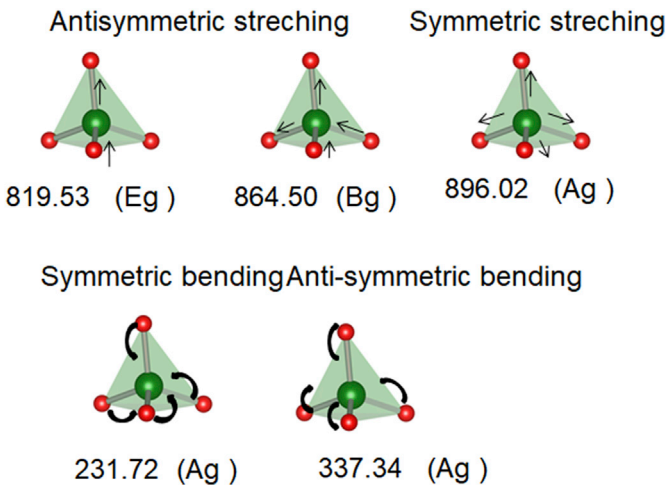

Fig. 4. Theoretical Raman-active modes of $CaMoO_4$.

3.5. Representations of the unit cell, surfaces, and cluster coordination

Fig. 5 shows a schematic representation of the tetragonal structure (space group $I4_1/a$) of the $CaMoO_4$ unit cell with atomic positions and lattice parameters obtained from the Rietveld refinement data (Tables 1 and 2) in which different clusters are depicted; that is, the local coordination of Ca and Mo atoms for the bulk (Fig. 5) and surfaces (Fig. 6).

In the bulk, Mo cations are coordinated by four oxygens, yielding [MoO_4] clusters with a tetrahedral configuration. These clusters are distorted because of the displaced positions of the O ions, yielding a variation in the O—Mo—O angles of the ideal tetrahedral configuration.

The (001), (112), (100), (110), (101), and (111) surfaces of $CaMoO_4$ were modeled by an unreconstructed slab model using an optimized equilibrium geometry. All surfaces are exposed to a vacuum by the Mo and O ions, while the Ca and O ions are the exposed centers on the (111) surface. In addition to the atomic configuration of the exposed facets, the coordination environment has a large effect on the stabilization of the surfaces. Since the bonding interaction of a Mo—O bond is stronger than that of a Ca—O bond, the stability of the (111) surface is reduced

Table 4
Optical band gap energy for $CaMoO_4$ without and with the surfactants ethyl 4-dimethylaminobenzoate (EDA) and 1,2,4,5-benzenetetracarboxylic dianhydride (BTD).

Samples	*t* (min)	E_{gap} (eV)
$CaMoO_4$	1	3.71
	2	3.71
	4	3.74
	8	3.75
$CaMoO_4$ (EDA)	1	3.51
	2	3.65
	4	3.66
	8	3.25
$CaMoO_4$ (BTD)	1	3.66
	2	3.71
	4	3.66
	8	3.68

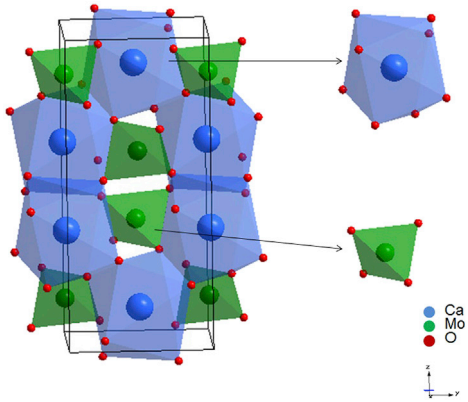

Fig. 5. The bulk structure of $CaMoO_4$, showing $[CaO_8]$ and $[MoO_4]$ clusters as building blocks of the material.

compared with that of the rest of the surfaces because of the presence of two oxygen vacancies; that is, under coordination at the $[MoO_2]$ cluster. Only the (112) surface presents $[CaO_5]$ clusters, implying a breaking of a Ca—O bond compared with the bulk.

The local coordination of the superficial Ca and Mo cations and the distance to the closer O ions are shown in Fig. 6.

3.6. Morphology study

Table 5 lists the surface energies, area, and relaxation energy during the optimization process for each surface. According to the DFT calculations, the stability of the surfaces is in the order (001)>(112)>(110)>(101)>(100)>(111).

These results can be explained in terms of local order (at short distance), taking into account the vacancies of the O ions in the superficial

Table 5
E_{surf}, area, and relaxation energy during the optimization process.

Surface	E_{surf} (J/m^2)	A (Å^2)	Relaxation energy (%)
(001)	0.72	27.385	14
(112)	0.75	50.054	70
(110)	0.93	41.898	70
(101)	1.01	32.637	74
(100)	1.15	59.253	43
(111)	4.56	88.157	1

Mo ($[MoO_4]$ and $[MoO_2]$) and Ca ($[CaO_6]$ and $[CaO_5]$) clusters. This information was used to map the available morphologies of $CaMoO_4$, assuming different values for the surface energy of different facets, and then the transformations between the different morphologies were associated with the relative surface energy of each surface. Fig. 7 illustrates the good agreement between the experimental FE-SEM images and the theoretical morphologies.

By modulating the relationship between the surface stabilities of the different faces, we obtained Fig. 7, which can be used to obtain correlations with the experimental results. This map displays the available morphologies of $CaMoO_4$ crystals resulting from a change in the relative stability of the facets. We started with the ideal morphology, and when the surface energies of the (001) and (101) surfaces increased, shape A was obtained (bottom of Fig. 7). When the surface energy of the (101) surface decreased, with simultaneous increase of the surface energy of (112) surfaces, shape B was obtained (top of Fig. 7). Other possibilities were observed when the surface energy of the (101) facet decreases and that of the (112) surface increases (middle of Fig. 7). Experimentally, EDA was determinant, because an interaction occurred on the structure, allowing two types of facets to be exposed in the resulting morphology. The experimental morphology was simulated by means of two paths: the first from shape A to shape A1, increasing the surface energy of the (001) surface to 1.37 J/m^2 and decreasing the corresponding value of the (100)

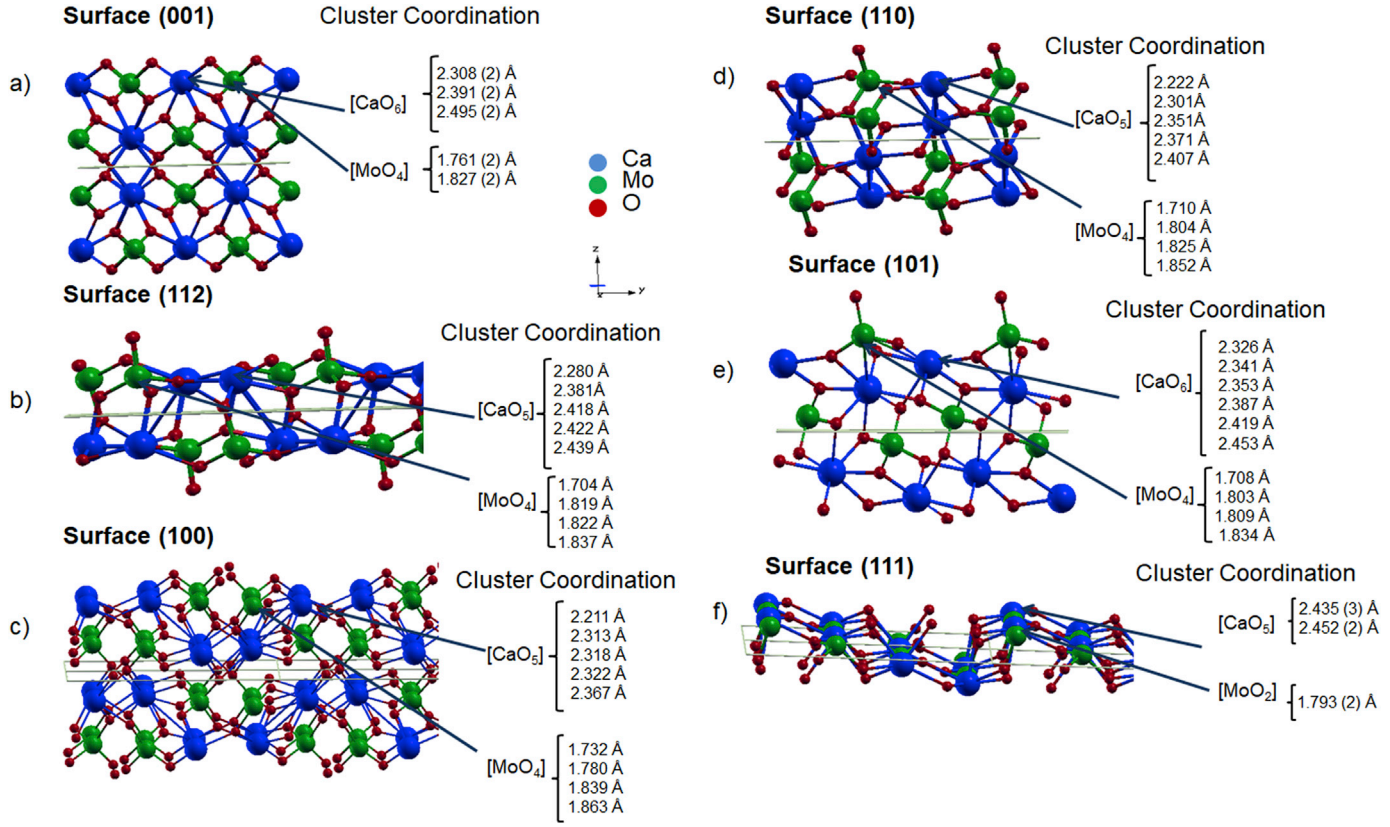

Fig. 6. The surfaces and Ca—O and Mo—O bond distances of the exposed atoms: (a) (001), (b) (112), (c) (100), (d) (110), (e) (101), and (f) (111).

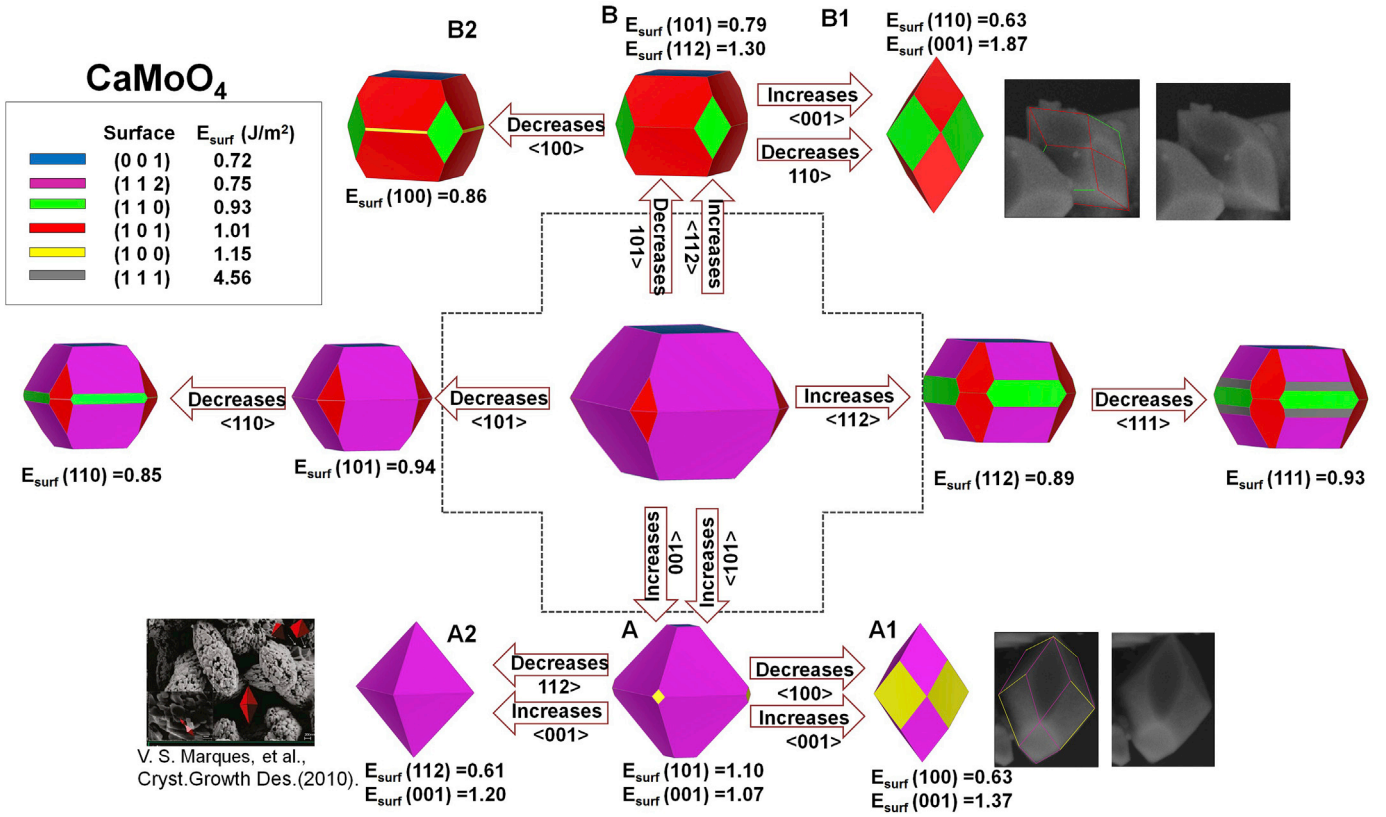

Fig. 7. Map of morphologies of $CaMoO_4$ with crystal planes (001), (112), (110), (101), (100), and (111).

surface to 0.63 J/m^2. The second path was obtained from shape B to shape B1, increasing the surface energy of the (001) surface to 1.87 J/m^2 and decreasing the corresponding value of the (110) surface to 0.63 J/m^2. The A2 morphology generated is similar to that synthesized by Ghaed-Amini et al. [91] and Marques et al. [2].

Therefore, the theoretical morphologies can be controlled by the different surface energies, and it is well known that morphologies can undergo changes because of differences in the environment in which they are synthesized. These differences may include the presence of surfactants and impurities, and differences in solvents, temperature, and synthetic routes.

3.7. Band structure and density of states

The computed band structure and total density of states (DOS) projected onto the atoms and orbitals of the $CaMoO_4$ structures, surfaces, and bulk are shown in Fig. 8.

An analysis of the DOS indicates that the upper part of the valence band consists mainly of O orbitals($2p_x$, $2p_y$ and $2p_z$) and lesser contributions of Ca and Mo orbitals. The lower part of the conduction band is derived mostly from Mo 4 d orbitals ($4d_z^2$, $4d_{x-y}^{22}$, $4d_{xy}$, $4d_{xz}$, $4d_{yz}$). The direct band gap energy of 4.92 eV (from Γ to Γ) is obtained for the bulk. An analysis of the projected DOS reveals that the top of the valance band is produced by a major contribution of the O $2p_z$ and $2p_z$ states, and the top of the conduction is due to Mo $4d_z^2$ states and minor contribution of $4d_{x-y}^{22}$ states (see Fig. 8(h)).

Calculations yielded a direct band gap energy for the (001), (112), (110), (101), and (100) surfaces very similar to that in the bulk crystal, with variations of 0.1–0.3 eV depending on the specific surface. However, the (111) surface has a conducting character, indicating a certain instability, possibly due to the breaking of coordination in [MoO_4] clusters with two vacancies.

3.8. PL analysis

The PL spectra of the $CaMoO_4$ as-synthesized powders with and without surfactants, (EDA and BTD) are shown in Fig. 9.

Broad emission bands associated with a multilevel process (i.e., involving the participation of numerous states within the band gap of the material [28]) can be observed.

Through the deconvolution of the PL spectra of pure $CaMoO_4$, $CaMoO_4$_EDA, and $CaMoO_4$_BTD (Fig. 9), it was possible to discovery three curves centered at 459 nm (blue), 529 nm (green), and 610 nm (orange), which covered all the visible electromagnetic spectrum. These results show the same behavior of PL for pure $CaMoO_4$ and $CaMoO_4$_EDA samples. On the other hand, $CaMoO_4$_BTD samples reveal an elevated percentage of the blue area, indicating a higher concentration of shallow defects than in pure $CaMoO_4$ and $CaMoO_4$_EDA samples, which favors equally the blue and green areas.

The blueshift in the PL is related to the changes in the morphology of the $CaMoO_4$ particles, from peanut-like for pure $CaMoO_4$ to spheres for $CaMoO_4$_EDA and dumbbell-like and flower-like for $CaMoO_4$_BTD (Fig. S7) and theoretical models (Fig. 7). However, other factors may also be involved in the PL, such as particle aggregation and differences in the size. On the other hand, we believe that the blueshift in $CaMoO_4$_BTD samples may be related to a preferential growth of the A1 structure described on the map of morphologies (Fig. 7), consequently promoting a higher concentration of shallow defects. Hence, the morphology and the PL in this study varied significantly with the heat treatment time, morphology, and surfactant used during the synthesis.

4. Conclusions

In summary, we have developed a morphology-controlled synthesis of $CaMoO_4$ crystals by means of a simple co-precipitation method and with

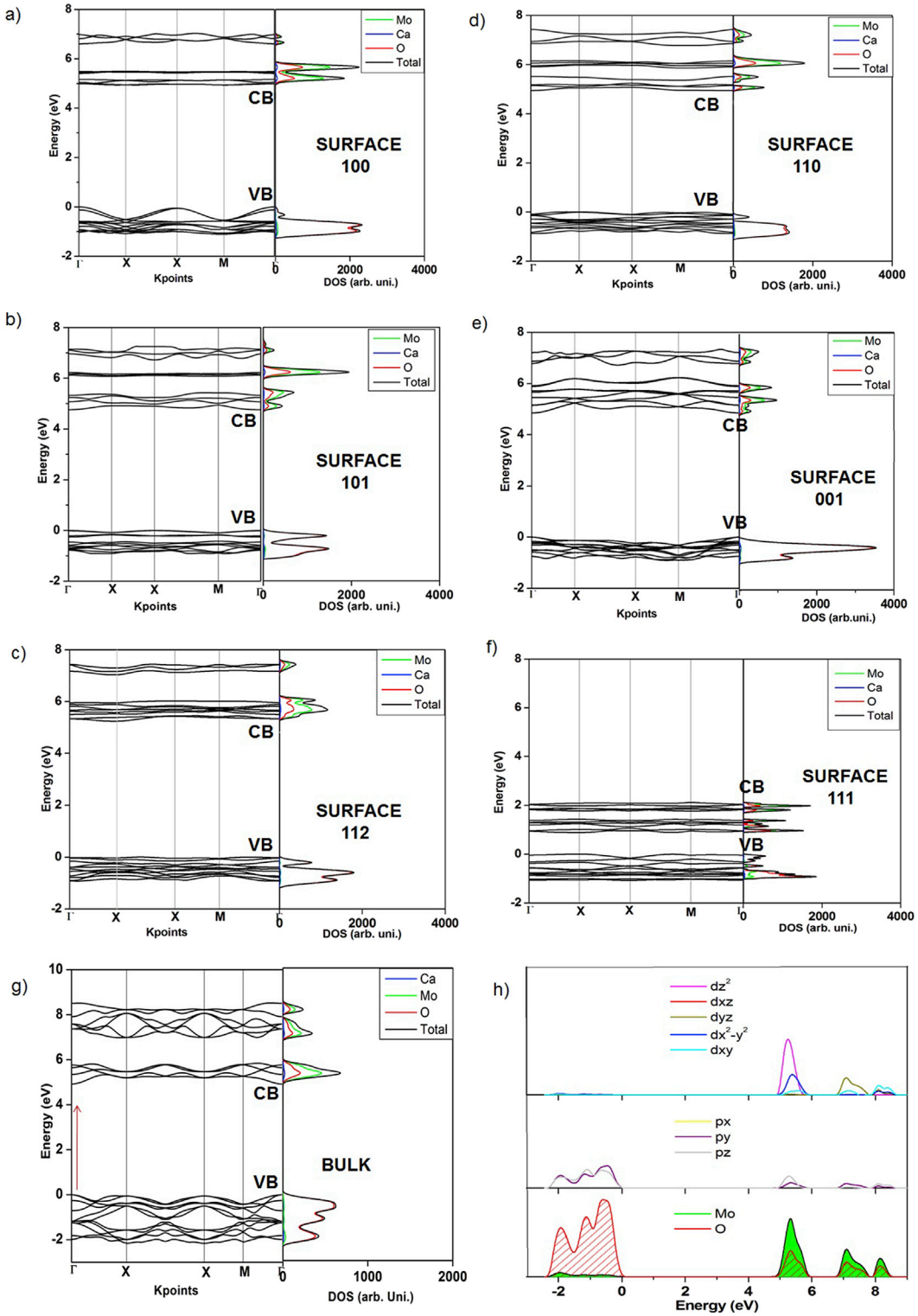

Fig. 8. Theoretical band structure and projected density of states (DOS): (a) the (100) surface, (b) the (101) surface, (c) the (112) surface, (d) the (110) surface, (e) the (001) surface, (f) the (111) surface, (g) bulk projected on atoms, and (h) bulk projected on orbitals.

processing in a domestic microwave-assisted hydrothermal system with and without use of different surfactants (EDA and BTD). The as-synthesized samples were characterized by XRD and Rietveld refinement techniques, FT-IR spectroscopy, UV–vis absorption spectroscopy, and PL measurements, while FE-SEM was used to investigate the morphology of the crystals. The effects of reaction conditions, including the presence of surfactant and reaction time, on the properties and morphology of $CaMoO_4$ were investigated systematically.

The available morphologies of $CaMoO_4$ comprise a complete array of polyhedral geometries that are achieved by modulation of the surface energies by use of a Wulff construction, and they can be fine-tuned to find the path to link the experimental morphologies (obtained by FE-SEM)

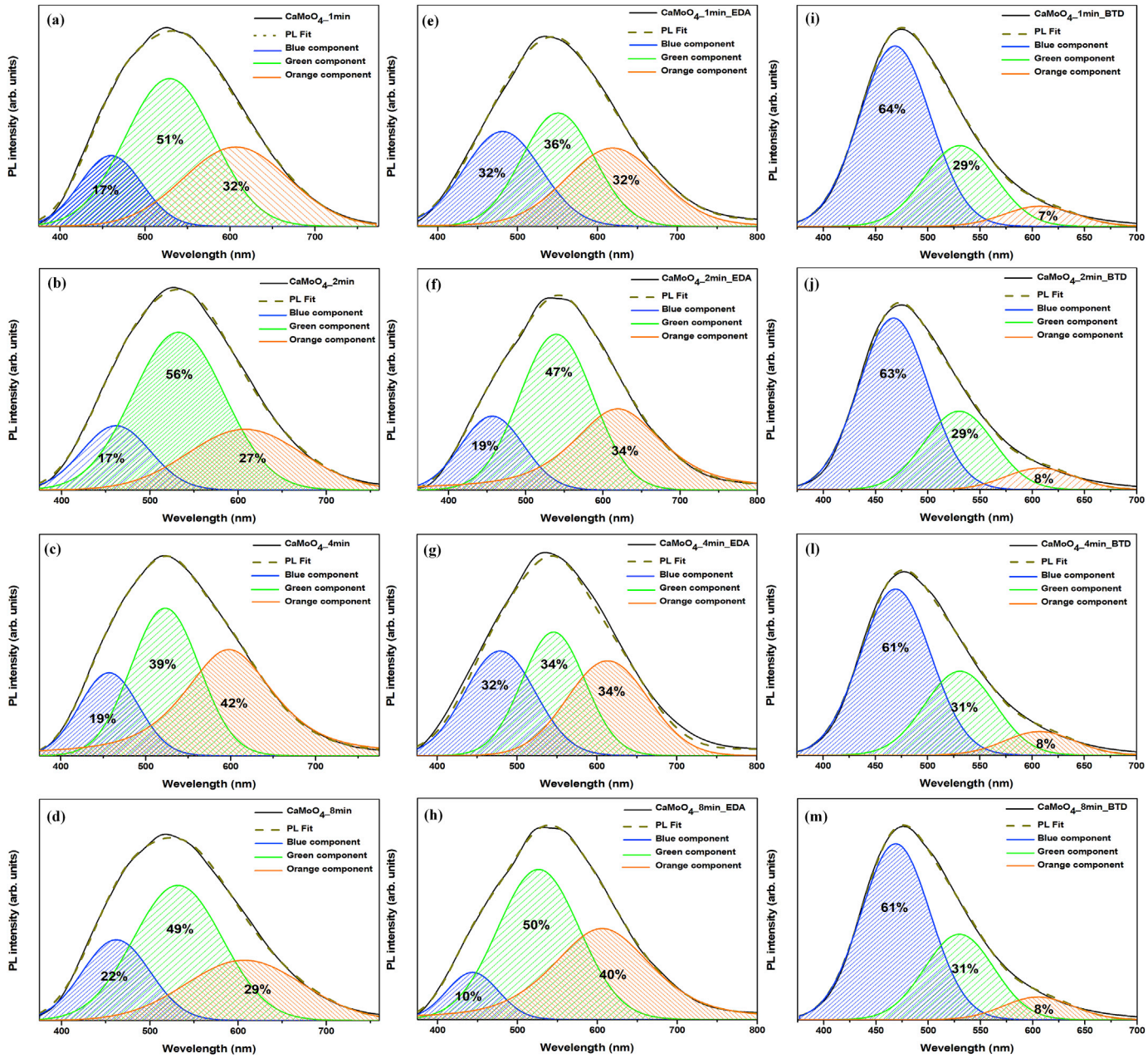

Fig. 9. Photoluminescence (PL) spectra patterns of $CaMoO_4$ microcrystals synthesized by the microwave-assisted hydrothermal method at 140 °C: (a) $CaMoO_4$ 1 min, (b) $CaMoO_4$ 2 min (c) $CaMoO_4$ 4 min, (d) $CaMoO_4$ 8 min, (e) $CaMoO_4$ prepared with ethyl 4-dimethylaminobenzoate ($CaMoO_4$_EAD) 1 min, (f) $CaMoO_4$_EAD 2 min (g) $CaMoO_4$_EAD 4 min, (h) $CaMoO_4$_EAD 8 min, (i) $CaMoO_4$ prepared with 1,2,4,5-benzenetetracarboxylic dianhydride ($CaMoO_4$_BTD) 1 min, (j) $CaMoO_4$_BTD 2 min, (l) $CaMoO_4$_BTD 4 min, and (m) $CaMoO_4$_BTD 8 min.

and theoretical morphologies. The surface energies for six different surfaces, (001), (112), (100), (110), (101), and (111), of the $CaMoO_4$ crystal were calculated with use of DFT. On the basis of the calculation results, the predominantly exposed surfaces in the morphologies of $CaMoO_4$ crystals and their morphological transformations were predicted. By tuning the surface energies, we obtained a complete map of the morphologies available for $CaMoO_4$, which enabled us to identify where the observed morphology from the FE-SEM images was located on this map. The experimental and theoretical morphologies obtained coincide when the surface energy of the (001) surface decreases and the surface energies of the (100) and (101) surfaces simultaneously increase. The present work is expected to catalyze more extensive studies on the different properties of this material. In particular, with the changes of experimental parameters that can be used for tuning the morphology of $CaMoO_4$ crystals, we anticipate that $CaMoO_4$ crystals with other exotic shapes will be unraveled in time. It is also likely that the concepts identified in this work can be extrapolated to the shape-controlled preparation of other related materials.

Acknowledgments

The authors thank the following Brazilian research financing institutions for financial support: National Council for Scientific and Technological Development - CNPq (Processo 402127/2013-7), São Paulo Research Foundation - FAPESP (Processo 2013/07296-2), Programa de Pós-Graduação em Ciência e Engenharia de Materiais (PPGCEM-UFRN), Generalitat Valenciana (PrometeoII/2014/022, ACOMP/2014/270, and ACOMP/2015/1202), Ministerio de Economía y

Competitividad, Spain (project CTQ2015-65207-P), and Programa de Cooperación Científica con Iberoamerica (Brazil) of the Ministerio de Educación, Spain (PHBP14-00020). J.A. acknowledges the Ministerio de Economia y Competitividad, "Salvador Madariaga" program, PRX15/00261. M.C.O acknowledges the Generalitat Valencia for the Santiago Grisolia program 2015/033.

Appendix A. Supplementary data

Supplementary data related to this article can be found at https://doi.org/10.1016/j.jpcs.2017.11.019.

References

[1] G. Botelho, I. Nogueira, E. Moraes, E. Longo, Study of structural and optical properties of $CaMoO_4$ nanoparticles synthesized by the microwave-assisted solvothermal method, Mater. Chem. Phys. 183 (2016) 110–120.
[2] V. Marques, L. Cavalcante, J. Sczancoski, A. Alcântara, M.O. Orlandi, E. Moraes, E. Longo, J.A. Varela, M. Siu Li, M. Santos, Effect of different solvent ratios (water/ethylene glycol) on the growth process of $CaMoO_4$ crystals and their optical properties, Cryst. Growth Des. 10 (2010) 4752–4768.
[3] A.K. Parchur, A.I. Prasad, A.A. Ansari, S.B. Rai, R.S. Ningthoujam, Luminescence properties of Tb3+-doped $CaMoO_4$ nanoparticles: annealing effect, polar medium dispersible, polymer film and core-shell formation, Dalton Trans. 41 (2012) 11032–11045.
[4] A.K. Parchur, R.S. Ningthoujam, Preparation and structure refinement of Eu3+ doped $CaMoO_4$ nanoparticles, Dalton Trans. 40 (2011) 7590–7594.
[5] W. Miller, C.W. Smith, D.S. Mackenzie, K.E. Evans, Negative thermal expansion: a review, J. Mater. Sci. 44 (2009) 5441–5451.
[6] F.A. Rabuffetti, S.P. Culver, L. Suescun, R.L. Brutchey, Structural disorder in $AMoO_4$ (A = Ca, Sr, Ba) scheelite nanocrystals, Inorg. Chem. 53 (2014) 1056–1061.
[7] S.P. Culver, R.L. Brutchey, Thermally activated rotational disorder in $CaMoO_4$ nanocrystals, CrystEngComm 18 (2016) 4485–4488.
[8] D. Gao, Y. Li, X. Lai, Y. Wei, J. Bi, Y. Li, M. Liu, Fabrication and luminescence properties of Dy^{3+} doped $CaMoO_4$ powders, Mater. Chem. Phys. 126 (2011) 391–397.
[9] J. Brübach, T. Kissel, M. Frotscher, M. Euler, B. Albert, A. Dreizler, A survey of phosphors novel for thermography, J. Lumin. 131 (2011) 559–564.
[10] J.H. Chung, S.Y. Lee, K.B. Shim, S.-Y. Kweon, S.-C. Ur, J.H. Ryu, Blue upconversion luminescence of $CaMoO_4$:Li^+/Yb^{3+}/Tm^{3+} phosphors prepared by complex citrate method, Appl. Phys. A 108 (2012) 369–373.
[11] J.H. Ryu, J.-W. Yoon, C.S. Lim, W.-C. Oh, K.B. Shim, Microwave-assisted synthesis of $CaMoO_4$ nano-powders by a citrate complex method and its photoluminescence property, J. Alloys Compd. 390 (2005) 245–249.
[12] D. Gao, X. Lai, C. Cui, P. Cheng, J. Bi, D. Lin, Oxidant-assisted preparation of $CaMoO_4$ thin film using an irreversible galvanic cell method, Thin Solid Films 518 (2010) 3151–3155.
[13] G. Li, Z. Wang, Z. Quan, C. Li, J. Lin, Growth of highly crystalline $CaMoO_4$:Tb^{3+} phosphor layers on spherical SiO_2 particles via sol-gel process: structural characterization and luminescent properties, Cryst. Growth Des. 7 (2007) 1797–1802.
[14] H. Wu, Y. Hu, W. Zhang, F. Kang, N. Li, G. Ju, Sol–gel synthesis of Eu3+ incorporated $CaMoO_4$: the enhanced luminescence performance, J. Sol-Gel Sci. Technol. 62 (2012) 227–233.
[15] Y. Zhang, L. Wang, D. Chu, H. Sun, A. Wang, Z. Ma, L. Yang, Y. Zhuang, Y. Bai, Fabrication of coupled twin-shaped hollow hemispherical calcium molybdate via a facile ultrasound-assisted approach, CrystEngComm 17 (2015) 2444–2449.
[16] S. Dutta, S. Som, S. Sharma, Luminescence and photometric characterization of K^+ compensated $CaMoO_4$:Dy^{3+} nanophosphors, Dalton Trans. 42 (2013) 9654–9661.
[17] Y.-S. Luo, X.-J. Dai, W.-D. Zhang, Y. Yang, C.Q. Sun, S.-Y. Fu, Controllable synthesis and luminescent properties of novel erythrocyte-like $CaMoO_4$ hierarchical nanostructures via a simple surfactant-free hydrothermal route, Dalton Trans. 39 (2010) 2226–2231.
[18] S.S. Hosseinpour-Mashkani, S.S. Hosseinpour-Mashkani, A. Sobhani-Nasab, Synthesis and characterization of rod-like $CaMoO_4$ nanostructure via free surfactant sonochemical route and its photocatalytic application, J. Mater. Sci. Mater. Electron. 27 (2016) 4351–4355.
[19] J. Liu, X. Huang, Y. Li, Z. Li, A general route to thickness-tunable multilayered sheets of sheelite-type metal molybdate and their self-assembled films, J. Mater. Chem. 17 (2007) 2754–2758.
[20] X. Choa, W. Ling, L. Hao, Z. Ding-Bing, Y. Tao-Kai, $CaMoO_4$ Hollow microspheres: ionic liquid-assisted synthesis and optical properties, Chin. J. Inorg. Chem. 23 (2007) 1941–1946.
[21] C. Xu, D. Zou, H. Guo, F. Jie, T. Ying, Luminescence properties of hierarchical $CaMoO_4$ microspheres derived by ionic liquid-assisted process, J. Lumin. 129 (2009) 474–477.
[22] P. Yu, G.-B. Hu, Y.-F. Tian, D.-Q. Xiao, Y. Liu, Q.-W. Guo, Synthesis and photoluminescent properties of nanocrystalline $CaMoO_4$ thin film via chemical solution processing, J. Nanosci. Nanotechnol. 8 (2008) 2651–2654.
[23] M. Laguna, N.O. Nunez, A.I. Becerro, M. Ocana, Morphology control of uniform $CaMoO_4$ microarchitectures and development of white light emitting phosphors by Ln doping (Ln = Dy^{3+}, Eu^{3+}), CrystEngComm 19 (2017) 1590–1600.
[24] Y.L. Yang, X.M. Li, W.L. Feng, W.L. Li, C.Y. Tao, Synthesis and characteristic of $CaMoO_4$: Eu^{3+} red phosphor for W-LED by co-precipitation, J. Inorg. Mater. 25 (2010) 1015.
[25] Y. Yang, X. Li, W. Feng, W. Yang, W. Li, C. Tao, Effect of surfactants on morphology and luminescent properties of $CaMoO_4$:Eu^{3+} red phosphors, J. Alloys Compd. 509 (2011) 845–848.
[26] T. Thongtem, S. Kungwankunakorn, B. Kuntalue, A. Phuruangrat, S. Thongtem, Luminescence and absorbance of highly crystalline $CaMoO_4$, $SrMoO_4$, $CaWO_4$ and $SrWO_4$ nanoparticles synthesized by co-precipitation method at room temperature, J. Alloys Compd. 506 (2010) 475–481.
[27] Y. Xiang, J. Song, G. Hu, Y. Liu, Synthesis of $CaMoO_4$ hierarchical structures via a simple slow-release co-precipitation method, Appl. Surf. Sci. 349 (2015) 374–379.
[28] V.M. Longo, L.S. Cavalcante, E.C. Paris, J.C. Sczancoski, P.S. Pizani, M.S. Li, J. Andrés, E. Longo, J.A. Varela, Hierarchical assembly of $CaMoO_4$ nano-octahedrons and their photoluminescence properties, J. Phys. Chem. C 115 (2011) 5207–5219.
[29] L. Wang, Y. Sun, C. Li, Y. Wang, X. Ma, Y. Wang, S. Li, Z. Zhang, P. Ma, G. Cui, Morphology-controlled $CaMoO_4$ nanorods via a facile microwave-assisted EDTA chelating agent process, Cryst. Res. Technol. 47 (2012) 1231–1236.
[30] Y. Sun, C. Li, Z. Zhang, X. Ma, L. Wang, Y. Wang, M. Song, P. Ma, L. Jiang, Y. Guo, Persimmon-like $CaMoO_4$ micro/nanomaterials: a rapid microwave-assisted fabrication, characterization, and the growth mechanism, Solid State Sci. 14 (2012) 219–224.
[31] A. Phuruangrat, T. Thongtem, S. Thongtem, Synthesis of nanocrystalline metal molybdates using cyclic microwave radiation, Mater. Sci. Pol. 28 (2010) 557–563.
[32] A. Phuruangrat, T. Thongtem, S. Thongtem, Preparation, characterization and photoluminescence of nanocrystalline calcium molybdate, J. Alloys Compd. 481 (2009) 568–572.
[33] T. Thongtem, A. Phuruangrat, S. Thongtem, Characterization of $MMoO_4$ (M = Ba, Sr and Ca) with different morphologies prepared using a cyclic microwave radiation, Mater. Lett. 62 (2008) 454–457.
[34] C. Bouzidi, K. Horchani-Naifer, Z. Khadraoui, H. Elhouichet, M. Ferid, Synthesis, characterization and DFT calculations of electronic and optical properties of $CaMoO_4$, Phys. B Condens. Matter 497 (2016) 34–38.
[35] T. Liu, J. Chen, F. Yan, Optical polarized properties related to the oxygen vacancy in the $CaMoO_4$ crystal, J. Lumin. 129 (2009) 101–104.
[36] C. Pu, T. Liu, Q. Zhang, Study of the electronic structures of $CaMoO_4$ crystal related to oxygen vacancy, Phys. Status Solidi (b) 245 (2008) 1586–1589.
[37] A.P. Kaushik, B. Lukose, P. Clancy, The role of shape on electronic structure and charge transport in faceted PbSe nanocrystals, ACS Nano 8 (2014) 2302–2317.
[38] N. Erdman, K.R. Poeppelmeier, M. Asta, O. Warschkow, D.E. Ellis, L.D. Marks, The structure and chemistry of the TiO_2-rich surface of $SrTiO_3$ (001), Nature 419 (2002) 55–58.
[39] B. Lv, Z. Liu, H. Tian, Y. Xu, D. Wu, Y. Sun, Single-crystalline dodecahedral and octodecahedral α-Fe_2O_3 particles synthesized by a fluoride anion–assisted hydrothermal method, Adv. Funct. Mater. 20 (2010) 3987–3996.
[40] H.G. Yang, C.H. Sun, S.Z. Qiao, J. Zou, G. Liu, S.C. Smith, H.M. Cheng, G.Q. Lu, Anatase TiO_2 single crystals with a large percentage of reactive facets, Nature 453 (2008) 638–641.
[41] W. Liu, J.-g. Wang, W. Li, X. Guo, L. Lu, X. Lu, X. Feng, C. Liu, Z. Yang, A shortcut for evaluating activities of TiO_2 facets: water dissociative chemisorption on TiO_2-B (100) and (001), Phys. Chem. Chem. Phys. 12 (2010) 8721–8727.
[42] J. Jiang, K. Zhao, X. Xiao, L. Zhang, Synthesis and facet-dependent photoreactivity of BiOCl single-crystalline nanosheets, J. Am. Chem. Soc. 134 (2012) 4473–4476.
[43] Z. Zongyan, L. Zhaosheng, Z. Zhigang, Surface properties and electronic structure of low-index stoichiometric anatase TiO_2 surfaces, J. Phys. Condens. Matter 22 (2010), 175008.
[44] Q. Gao, Y.-M. Ju, D. An, M.-R. Gao, C.-H. Cui, J.-W. Liu, H.-P. Cong, S.-H. Yu, Shape-controlled synthesis of monodisperse PdCu nanocubes and their electrocatalytic properties, ChemSusChem 6 (2013) 1878–1882.
[45] L. Wang, S. Zhao, C. Liu, C. Li, X. Li, H. Li, Y. Wang, C. Ma, Z. Li, J. Zeng, Aerobic oxidation of cyclohexane on catalysts based on twinned and single-crystal $Au_{75}Pd_{25}$ bimetallic nanocrystals, Nano Lett. 15 (2015) 2875–2880.
[46] H. Lee, S.E. Habas, S. Kweskin, D. Butcher, G.A. Somorjai, P. Yang, Morphological control of catalytically active platinum nanocrystals, Angew. Chem. Int. Ed. 45 (2006) 7824–7828.
[47] T.S. Ahmadi, Z.L. Wang, T.C. Green, A. Henglein, M.A. El-Sayed, Shape-controlled synthesis of colloidal platinum nanoparticles, Science 272 (1996) 1924–1925.
[48] X.-F. Wang, G.-H. Peng, N. Li, Z.-H. Liang, X. Wang, J.-L. Wu, Hydrothermal synthesis and luminescence properties of 3D walnut-like CaMoO 4: Eu 3+ red phosphors, J. Alloys Compd. 599 (2014) 102–107.
[49] V.D. Araújo, R.L. Tranquilin, F.V. Motta, C.A. Paskocimas, M.I.B. Bernardi, L.S. Cavalcante, J. Andrés, E. Longo, M.R.D. Bomio, Effect of polyvinyl alcohol on the shape, photoluminescence and photocatalytic properties of $PbMoO_4$ microcrystals, Mater. Sci. Semicond. Process. 26 (2014) 425–430.
[50] A. Ruditskiy, H.-C. Peng, Y. Xia, Shape-controlled metal nanocrystals for heterogeneous catalysis, Annu. Rev. Chem. Biomol. Eng. 7 (2016) 327–348.
[51] J. Andrés, G. Lourdes, G. Amanda Fernandes, F. Mateus Meneghetti, L. Elson, Effects of surface stability on the morphological transformation of metals and metal oxides as investigated by first-principles calculations, Nanotechnology 26 (2015), 405703.
[52] M.M. Ferrer, A.F. Gouveia, L. Gracia, E. Longo, J. Andrés, A 3D platform for the morphology modulation of materials: first principles calculations on the thermodynamic stability and surface structure of metal oxides: Co_3O_4, α-Fe_2O_3, and In_2O_3, Model. Simul. Mater. Sci. Eng. 24 (2016), 025007.
[53] G.S. Silva, L. Gracia, M.T. Fabbro, L.P. Serejo dos Santos, H. Beltrán-Mir, E. Cordoncillo, E. Longo, J. Andrés, Theoretical and experimental insight on

Ag_2CrO_4 microcrystals: synthesis, characterization, and photoluminescence properties, Inorg. Chem. 55 (2016) 8961–8970.
[54] A.F. Gouveia, M.M. Ferrer, J.R. Sambrano, J. Andrés, E. Longo, Modeling the atomic-scale structure, stability, and morphological transformations in the tetragonal phase of $LaVO_4$, Chem. Phys. Lett. 660 (2016) 87–92.
[55] M.C. Oliveira, L. Gracia, I.C. Nogueira, M.F.C. Gurgel, J.M.R. Mercury, E. Longo, J. Andrés, Synthesis and morphological transformation of $BaWO_4$ crystals: experimental and theoretical insights, Ceram. Inter. 42 (2016) 10913–10921.
[56] M.C. Oliveira, L. Gracia, I.C. Nogueira, M.F.C. Gurgel, J.M.R. Mercury, E. Longo, J. Andrés, On the morphology of $BaMoO_4$ crystals: a theoretical and experimental approach, Cryst. Res. Technol. 51 (2016) 634–644.
[57] R.C. de Oliveira, C.C. de Foggi, M.M. Teixeira, M.D.P. da Silva, M. Assis, E.M. Francisco, B.N.A.d.S. Pimentel, P.F.d.S. Pereira, C.E. Vergani, A.L. Machado, J. Andrés, L. Gracia, E. Longo, Mechanism of antibacterial activity via morphology change of α-$AgVO_3$: theoretical and experimental insights, ACS Appl. Mater. Interfaces 9 (13) (2017) 11472–11481.
[58] C.H.B. Ng, W.Y. Fan, Crystal origami: preparation of β-Ag_2MoO_4 concave and convex crystals with high-index facets, ChemNanoMat 3 (2017) 178–182.
[59] S. Ishihara, N. Iyi, Y. Tsujimoto, S. Tominaka, Y. Matsushita, V. Krishnan, M. Akada, J. Labuta, K. Deguchi, S. Ohki, M. Tansho, T. Shimizu, Q. Ji, Y. Yamauchi, J.P. Hill, H. Abe, K. Ariga, Hydrogen-bond-driven 'homogeneous intercalation' for rapid, reversible, and ultra-precise actuation of layered clay nanosheets, Chem. Commun. 49 (2013) 3631–3633.
[60] A.K. Parchur, A.A. Ansari, B.P. Singh, T.N. Hasan, N.A. Syed, S.B. Rai, R.S. Ningthoujam, Enhanced luminescence of CaMoO4:Eu by core@shell formation and its hyperthermia study after hybrid formation with Fe3O4: cytotoxicity assessment on human liver cancer cells and mesenchymal stem cells, Integr. Biol. 6 (2014) 53–64.
[61] A. Khorsand Zak, W.H. Abd Majid, M.E. Abrishami, R. Yousefi, X-ray analysis of ZnO nanoparticles by Williamson–Hall and size–strain plot methods, Solid State Sci. 13 (2011) 251–256.
[62] A.D. Becke, Density-functional thermochemistry. III. The role of exact exchange, J. Chem. Phys. 98 (1993) 5648–5652.
[63] C. Lee, W. Yang, R.G. Parr, Development of the Colle-Salvetti correlation-energy formula into a functional of the electron density, Phys. Rev. B 37 (1988) 785.
[64] R. Dovesi, R. Orlando, A. Erba, C.M. Zicovich-Wilson, B. Civalleri, S. Casassa, L. Maschio, M. Ferrabone, M. De La Pierre, P. D'Arco, Y. Noël, M. Causà, M. Rérat, B. Kirtman, CRYSTAL14: a program for the ab initio investigation of crystalline solids, Int. J. Quantum Chem. 114 (2014) 1287–1317.
[65] http://www.crystal.unito.it/Basis_Sets/Molibdenum.Html, Molibdenum basis-sets.
[66] http://www.crystal.unito.it/Basis_Sets/Oxygen.Html, Oxygen basis-sets.
[67] L. Valenzano, F.J. Torres, K. Doll, F. Pascale, C.M. Zicovich-Wilson, R. Dovesi, Ab initio study of the vibrational spectrum and related properties of crystalline compounds; the case of $CaCO_3$ calcite, Zeitschrift für Physikalische Chemie 220 (2006) 893–912.
[68] H.J. Monkhorst, J.D. Pack, Special points for Brillouin-zone integrations, Phys. Rev. B 13 (1976) 5188.
[69] G. Wulff, Xxv. Zur Frage der Geschwindigkeit des Wachsthums und der Auflösung der Krystallflächen, Zeitschrift für Kristallographie-Crystalline Materials 34 (1901) 449–530.
[70] M. Bomio, R. Tranquilin, F. Motta, C. Paskocimas, R. Nascimento, L. Gracia, J. Andrés, E. Longo, Toward understanding the photocatalytic activity of $PbMoO_4$ powders with predominant (111),(100),(011), and (110) facets. A combined experimental and theoretical study, J. Phys. Chem. C 117 (2013) 21382–21395.
[71] V.M. Longo, L. Gracia, D.G. Stroppa, L.S. Cavalcante, M. Orlandi, A.J. Ramirez, E.R. Leite, J. Andrés, A. Beltrán, J.A. Varela, A joint experimental and theoretical study on the nanomorphology of $CaWO_4$ crystals, J. Phys. Chem. C 115 (2011) 20113–20119.
[72] G. Botelho, J. Andrés, L. Gracia, L.S. Matos, E. Longo, Photoluminescence and photocatalytic properties of Ag_3PO_4 microcrystals: an experimental and theoretical investigation, ChemPlusChem 81 (2016) 202–212.
[73] M.T. Fabbro, C. Saliby, L.R. Rios, F.A. La Porta, L. Gracia, M.S. Li, J. Andrés, L.P. Santos, E. Longo, Identifying and rationalizing the morphological, structural, and optical properties of-Ag_2MoO_4 microcrystals, and the formation process of Ag nanoparticles on their surfaces: combining experimental data and first-principles calculations, Sci. Technol. Adv. Mater. 16 (6) (2015 Dec) 065002–065012.
[74] M.C. Oliveira, L. Gracia, I.C. Nogueira, M.F.C. Gurgel, J.M.R. Mercury, E. Longo, J. Andrés, Synthesis and morphological transformation of $BaWO_4$ crystals: experimental and theoretical insights, Ceram. Int. 42 (2016) 10913–10921.
[75] G.S. Silva, L. Gracia, M.T. Fabbro, L.P. Serejo dos Santos, H. Beltrán-Mir, E. Cordoncillo, E. Longo, J. Andrés, Theoretical and experimental insight on Ag_2CrO_4 microcrystals: synthesis, characterization, and photoluminescence properties, Inorg. Chem. 55 (2016) 8961–8970.
[76] P.D. File, Joint Committee on Powder Diffraction Standards, ASTM, Philadelphia, Pa, 1967, pp. 9–185.
[77] R. Roca, J.C. Sczancoski, I.C. Nogueira, M.T. Fabbro, H. Alves, L. Gracia, L.P. Santos, C. De Sousa, J. Andrés, G. Luz, Facet-dependent photocatalytic and antibacterial properties of α-Ag_2WO_4 crystals: combining experimental data and theoretical insights, Catal. Sci. Technol. 5 (2015) 4091–4107.
[78] L. Lutterotti, S. Matthies, H.R. Wenk, Maud, Materials analysis using diffraction, Newsl. CPD 21 (1999) 14–15.
[79] H. Rietveld, A profile refinement method for nuclear and magnetic structures, J. Appl. Crystallogr. 2 (1969) 65–71.
[80] S. Gražulis, A. Daškevič, A. Merkys, D. Chateigner, L. Lutterotti, M. Quirós, N.R. Serebryanaya, P. Moeck, R.T. Downs, A. Le Bail, Crystallography Open Database (COD): an open-access collection of crystal structures and platform for world-wide collaboration, Nucleic Acids Res. 40 (2011) D420–D427.
[81] S.P.S. Porto, J.F. Scott, Raman spectra of $CaWO_4$, $SrWO_4$, $CaMoO_4$, and $SrMoO_4$, Phys. Rev. 157 (1967) 716–719.
[82] A. Marques, F. Motta, E. Leite, P. Pizani, J.A. Varela, E. Longo, D. De Melo, Evolution of photoluminescence as a function of the structural order or disorder in $CaMoO_4$ nanopowders, J. Appl. Phys. 104 (2008), 043505.
[83] M. Nicol, J.F. Durana, Vibrational Raman spectra of $CaMoO_4$ and $CaWO_4$ at high pressures, J. Chem. Phys. 54 (1971) 1436–1440.
[84] P.G. Zverev, Vibronic relaxation of Raman modes in $CaMoO_4$ and $PbMoO_4$ molecular ionic crystals, Phys. status solidi C. 1 (2004) 3101–3105.
[85] V.M. Longo, A.T.d. Figueiredo, A.B. Campos, J.W. Espinosa, A.C. Hernandes, C. Taft, J.R. Sambrano, J.A. Varela, E. Longo, Different origins of green-light photoluminescence emission in structurally ordered and disordered powders of calcium molybdate, J. Phys. Chem. A 112 (2008) 8920–8928.
[86] E. Sarantopoulou, C. Raptis, S. Ves, D. Christofilos, G.A. Kourouklis, Temperature and pressure dependence of Raman-active phonons of $CaMoO_4$: an anharmonicity study, J. Phys. Condens. Matter 14 (2002) 8925.
[87] T.T. Basiev, A.A. Sobol, Y.K. Voronko, P.G. Zverev, Spontaneous Raman spectroscopy of tungstate and molybdate crystals for Raman lasers, Opt. Mater. 15 (2000) 205–216.
[88] D.L. Wood, J. Tauc, Weak Absorption tails in amorphous semiconductors, Phys. Rev. B 5 (1972) 3144–3151.
[89] R.A. Roca, J.C. Sczancoski, I.C. Nogueira, M.T. Fabbro, H.C. Alves, L. Gracia, L.P.S. Santos, C.P. de Sousa, J. Andrés, G.E. Luz, E. Longo, L.S. Cavalcante, Facet-dependent photocatalytic and antibacterial properties of α-Ag_2WO_4 crystals: combining experimental data and theoretical insights, Catal. Sci. Technol. 5 (2015) 4091–4107.
[90] J.C. Sczancoski, M.D.R. Bomio, L.S. Cavalcante, M.R. Joya, P.S. Pizani, J.A. Varela, E. Longo, M.S. Li, J.A. Andrés, Morphology and blue photoluminescence emission of $PbMoO_4$ processed in conventional hydrothermal, J. Phys. Chem. C 113 (2009) 5812–5822.
[91] M. Ghaed-Amini, M. Bazarganipour, M. Salavati-Niasari, Calcium molybdate octahedral nanostructures, hierarchical self-assemblies controllable synthesis by coprecipitation method: characterization and optical properties, J. Ind. Eng. Chem. 21 (2015) 1089–1097.